#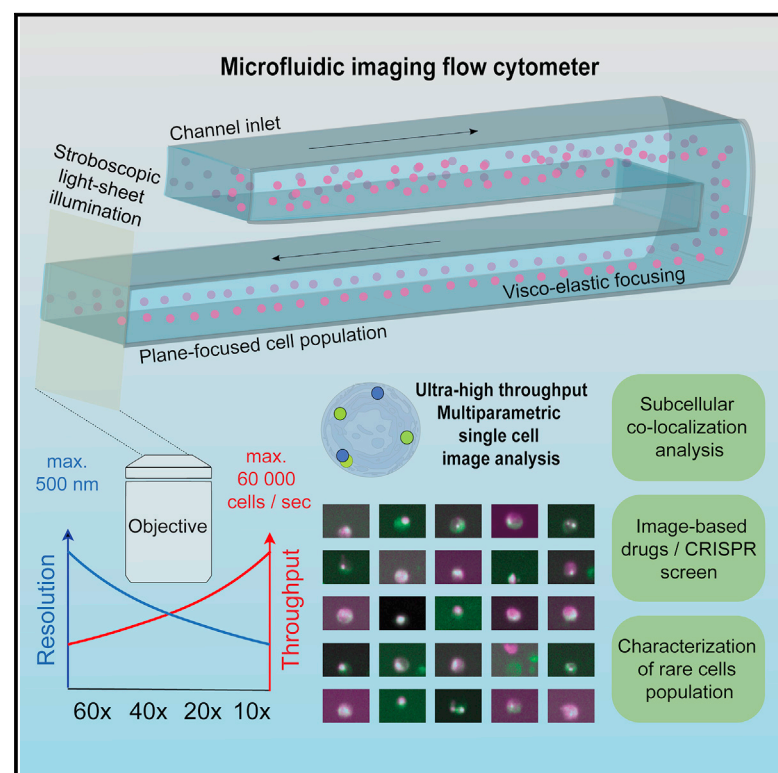 High-throughput multiparametric imaging flow cytometry: toward diffraction-limited sub-cellular detection and monitoring of sub-cellular processes

Graphical Abstract

Authors

Gregor Holzner, Bogdan Mateescu, Daniel van Leeuwen, Gea Cereghetti, Reinhard Dechant, Stavros Stavrakis, Andrew deMello

Correspondence

stavros.stavrakis@chem.ethz.ch (S.S.), andrew.demello@chem.ethz.ch (A.d.)

In brief

Holzner et al. describe a microfluidic imaging flow cytometer that incorporates stroboscopic illumination for blur-free fluorescence detection, enabling sub-cellular multi-color analysis at throughputs above 60,000 cells/s. This imaging platform notably enables ultra-high-throughput colocalization analysis of fluorescent proteins within phase-separated compartments at a resolution down to 500 nm in eukaryotic cells.

Highlights

- A high-throughput (60,000 cells/s) method for fluorescence imaging flow cytometry

- Collection of multi-color fluorescence blur-free images with high sensitivity

- Sub-cellular analysis of structures down to 500 nm with microscopy image quality

- High-throughput localization analysis of phase-separated compartments in cells

Cell Reports

Resource

High-throughput multiparametric imaging flow cytometry: toward diffraction-limited sub-cellular detection and monitoring of sub-cellular processes

Gregor Holzner,[1,5] Bogdan Mateescu,[2,5] Daniel van Leeuwen,[3] Gea Cereghetti,[4] Reinhard Dechant,[4] Stavros Stavrakis,[1,*] and Andrew deMello[1,6,*]

[1]Institute for Chemical & Bioengineering, ETH Zürich, Vladimir Prelog Weg 1, 8093 Zürich, Switzerland
[2]Brain Research Institute, University of Zurich, Winterthurerstrasse 190, 8057 Zurich, Switzerland
[3]Department of Biology, ETH Zürich, Universitätstrasse 2, 8092 Zurich, Switzerland
[4]Institute of Biochemistry, ETH Zürich, Otto-Stern-Weg 3, 8093 Zürich, Switzerland
[5]These authors contributed equally
[6]Lead contact
*Correspondence: stavros.stavrakis@chem.ethz.ch (S.S.), andrew.demello@chem.ethz.ch (A.d.)
https://doi.org/10.1016/j.celrep.2021.108824

SUMMARY

We present a sheathless, microfluidic imaging flow cytometer that incorporates stroboscopic illumination for blur-free fluorescence detection at ultra-high analytical throughput. The imaging platform is capable of multi-parametric fluorescence quantification and sub-cellular localization of these structures down to 500 nm with microscopy image quality. We demonstrate the efficacy of the approach through the analysis and localization of P-bodies and stress granules in yeast and human cells using fluorescence and bright-field detection at analytical throughputs in excess of 60,000 and 400,000 cells/s, respectively. Results highlight the utility of our imaging flow cytometer in directly investigating phase-separated compartments within cellular environments and screening rare events at the sub-cellular level for a range of diagnostic applications.

INTRODUCTION

Flow cytometry is widely recognized as the gold-standard technique for the analysis and enumeration of heterogeneous cellular populations and has become an indispensable tool in diagnostics (Hasegawa et al., 2013), rare-cell detection (Boraldi et al., 2016), and single cell proteomics (Gauthier et al., 2008). Although contemporary flow cytometers are able to analyze many thousands of cells per second, with classification based on scattering or fluorescence criteria, the vast majority require the processing of unacceptably large sample volumes and do not allow the acquisition of spatially resolved information.

Imaging flow cytometry (IFC) is a hybrid technology, incorporating the advantages of microscopy and flow cytometry, for high-throughput imaging of cells within flowing environments. Such an approach provides for enormous enhancements in information content but is accompanied by a number of technological challenges, including the need to acquire high-resolution (blur-free) images of single cells moving at high speed, the integration of multiple imaging modes (such as fluorescence, bright-field, and dark-field imaging) and the realization of adequate detection sensitivities when using short exposure times (Basiji et al., 2007). Commercial imaging flow cytometers (notably, the Amnis ImageStream X) have been shown to be successful in capturing images of single cells in flow (Barteneva et al., 2012). Through the use of hydrodynamic focusing, wide-field sample excitation, and time delay and integration charge-coupled device (TDI-CCD) image sensors, such systems can provide

high-resolution and multiplexed imaging capabilities at the expense of low to moderate throughput (i.e., up to 5,000 cells/s at 20× magnification) (Basiji et al., 2007). Significantly, imaging flow cytometers have been used to good effect in the detection and analysis of tumor cells (van Beers et al., 2014; Hui et al., 2014), notably in acute leukemia (Grimwade et al., 2017). Compared with traditional (single-point) flow cytometry techniques, an imaging capability allows the detection of chromosomal signaling, antigen localization, and other events that occur within the cell (van Beers et al., 2014; Grimwade et al., 2017). Finally, it should also be noted that imaging cells in flow avoids the requirements of membrane staining, which is especially important for performing image segmentation under static conditions (Berchtold et al., 2018).

As noted, a key drawback associated with conventional imaging flow cytometers is their low analytical throughput (typically between 2,000 and 3,000 cells/s at 20× magnification); more than one order of magnitude lower than non-imaging flow cytometers. Accordingly, a major challenge is to ensure high-detection sensitivities while also achieving high-analytical throughput. High-throughput imaging can be used to provide significant biological insight in the quantitative analysis of blood. A good example in this respect is the discrimination of leucocyte subsets via cellular DNA fluorescence analysis. Leucocyte sub-populations can be discriminated using the IFC approach because of their high-internal complexity and variations in cell size. Indeed, in contrast to neutrophils, lymphocytes are small and exhibit low internal complexity (López-Riquelme et al., 2013). To this end,
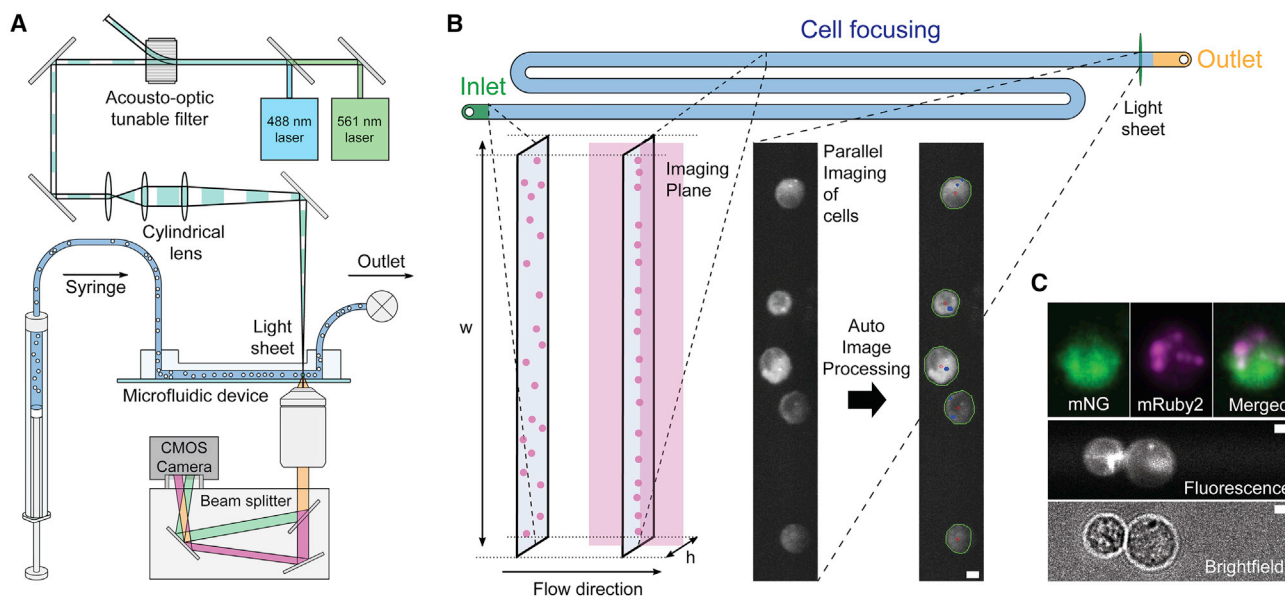
Figure 1. High-throughput multiparametric imaging flow cytometry

(A) The imaging flow cytometry platform integrates stroboscopic multi-color light sheet illumination, a microfluidic cell focusing system, a dual-color beam splitter, and a CMOS camera.

(B) Top view of the microfluidic channel used to position the cells in the imaging plane. The microfluidic device consists of a straight, high-aspect ratio channel with one inlet and one outlet. Through the use of a viscoelastic carrier fluid, cells can be precisely focused in the center plane of the channel. Cells are imaged upstream of the outlet using stroboscopic light sheet illumination, with image processing being used for cell identification and spot foci counting.

(C) Representative dual-color fluorescence images of 293T cells expressing mNeonGreen (mNG) (left, top) and mRuby2 (middle, top) tagged proteins. The corresponding merged image is shown in the top right panel. Images in the lower two panels show the simultaneous acquisition of fluorescence and bright-field images at high-throughput. Scale bars, 5 μm.

recent studies have leveraged the capabilities of microfluidic systems to manipulate, order, and process micrometer-sized objects in a controlled and high-throughput manner. For example, Rane et al. (2017) recently presented an imaging flow cytometer integrating inertial focusing (for the sheathless manipulation of cells) and stroboscopic fluorescence imaging for the analysis of large numbers of rapidly moving cells, with a maximum imaging throughput of 50,000 cells/s. However, use of a 10× objective restricted imaging resolution to above the diffraction limit. Moreover, Miura et al. (2018) reported the use of light sheet excitation of flowing cells within a mirror-embedded microfluidic device. Such a platform was used to extract fluorescence images of rapidly moving adenocarcinoma cells at throughputs approaching 10,000 cells/s. Instead of using CCD cameras for imaging, images can also be reconstructed from photomultiplier tube (PMT) signals through spatiotemporal transformation. In this way, Han and Lo (2015) produced high-resolution fluorescence and scatter-based images of moving cells at a throughput of approximately 1,000 cells/s. To preserve image quality when cells are moving at high-linear velocities, a free-space pulse-stretching method called free-space angular-chirp-enhanced delay (FACED) (Wu et al., 2017) has recently been used for time-stretch imaging, as well as for fluorescence imaging of rapidly moving beads (Goda et al., 2012). Additionally, laser-scanning confocal fluorescence microscopy based on frequency-division multiplexing has been used for high-throughput confocal fluorescence imaging of cells at frame rates of 16,000

frames/s (Mikami et al., 2018). More recently, a deep-learning-assisted, image-activated cell sorting platform reported real-time single-cell sorting of microalgal and blood cells on the basis of intracellular protein localization (Nitta et al., 2018). That said, it should be noted that all the above platforms, in addition to requiring exotic and often complex optical hardware, have only been used to report gross morphological features, such as cell/nucleus areas and perimeters. Indeed, the localization of sub-cellular features equal to or less than 1 μm in size (with microscopy image quality) and at throughputs in excess of 10,000 cells/s has yet to be reported. To this end, we herein present a high-throughput imaging flow cytometer (Figure 1) capable of multiparametric imaging (multi-color fluorescence and bright-field analysis), accurate cell sizing, and, most important, sub-cellular localization detection of features close to the diffraction limit. To demonstrate utility, we apply the developed platform to the ultra-high-throughput localization of sub-micrometer sub-cellular structures in both yeast and human cells.

RESULTS

Microfluidic design and characterization of cell focusing

The performance of our IFC platform was showcased through high-throughput quantitative imaging analysis of cytoplasmic RNA granules in yeast (stress granules) and human cells (P-bodies). To afford acquisition rates in excess of 10,000 cells/s, we combined stroboscopic illumination, a technique able to

Table 1. Performance characteristics of the imaging flow cytometers

Stroboscopic imaging flow cytometer				
Magnification	40×	20×	15×	10×
Numerical aperture	0.75	0.5	0.5	0.5
Pixel size, μm	0.16 × 0.16	0.33 × 0.33	0.43 × 0.43	0.65 × 0.65
Field of view, μm	332 × 25	665 × 25	887 × 25	1331 × 25
Imaging rate, cells/s	5,350	10,900	20,500	61,000
ImageStream Mark II imaging flow cytometer				
Magnification	60×	40×	20×	
Numerical aperture	0.9	0.75	0.5	
Pixel size, μm	0.3 × 0.3	0.5 × 0.5	1 × 1	
Field of view, μm	40 × 170	60 × 128	120 × 256	
Imaging rate, cells/s	1,200	2,000	4,000	

generate blur-free images of objects moving at high-linear velocities (Rane et al., 2017), with elasto-inertial three-dimensional (3D) cell focusing (Holzner et al., 2017, 2018) to provide for enhanced control of both flow velocities and cell position within the axial depth of focus of the objective lens (Figures 1A and 1B; Figures S1A and S1B). A schematic of the microfluidic device is shown in Figure 1B, consisting of a single high-aspect ratio channel. The microfluidic flow path is simple in construction, incorporating a single channel (90 mm long, 665 μm wide, and 59 μm deep) containing two switchbacks and an imaging zone located close to the outlet. Typically, parallel microfluidic geometries require precise distribution of cells among all channels. This can be challenging, as cells must be uniformly distributed to maximize throughput. The use of only a single microfluidic channel avoids problems associated with evenly distributing sample across multiple channels. This in turn removes imaging losses due to finite inter-channel spacing in the field of view, minimizes channel blockages due to small cross sections, and leads to significant increases in analytical throughput. Additionally, it is important to note that elasto-inertial focusing provides for control over the axial position of cells within the microfluidic channel and operates within a lower flow rate regime than related inertial focusing schemes (Di Carlo et al., 2007). These features are ideal for high-resolution IFC, as signal collection can be achieved using longer exposure times. Multiparametric detection involves both bright-field imaging, for sizing and morphology measurements and multi-color fluorescence detection, for sub-cellular localization detection (Figure 1C; Video S1).

Single-plane focusing of cells (Figures S1A and S1B) was achieved through use of a viscoelastic polyethylene oxide (PEO) carrier solution. Figure S1A presents images of 10 μm PS beads immersed in either deionized (DI) water or 1,000 ppm, 0.4 MDa PEO carrier fluid, moving at a volumetric flow rate of 360 μL/min. For water, and under inertial flow conditions, beads are focused into two planes (labeled A and B) (Di Carlo et al., 2007). However, when using a viscoelastic carrier fluid, all particles are focused to the center plane of the channel. To confirm single-plane focusing at the center of the channel cross section, bead intensities in the z direction were measured using a spinning disk confocal microscope and are presented in Figure S1B.

An important aspect when imaging cells moving at high-linear velocities is maintenance of a homogeneous flow profile across the channel width. Such a profile guarantees that the cells move across the imaging region at a uniform speed, thus ensuring correct sampling. To assess the uniformity of flow profiles across the channel, flow velocities were measured using bright-field imaging. Flow profiles of cells suspended in 0.4 MDa, 500 ppm PEO and 1 MDa, 500 ppm PEO solutions and moving at velocities between 0.01 and 0.25 m/s were recorded and are shown in Figure S1C. For all flow rates, the corresponding flow velocity profiles are homogeneous across the channel and, as expected, bend slightly toward the channel walls. Examination of two different molecular weight PEO solutions over a wide range of flow rates indicates that focusing at the channel centerline remains efficient when using a low-molecular weight PEO (1 MDa) solution at flow rates between 0.01 and 0.1 m/s (Figure S1D). Computational fluid dynamics simulations were further used to confirm experimental observations of flow distribution uniformity in the region where cells enter the microchannel (Figure S1E). Significantly, the coefficient of variation (CV) of the mean velocity along the detection channel is negligible (<0.99%), confirming a uniform flow distribution throughout the entire microfluidic device.

Analytical throughput and sensitivity

To eliminate motion blur when imaging rapidly moving cells, we stroboscopically manipulated the excitation beam between 10 and 20 μs. This allowed precise cell segmentation (Figure S2A) and extraction of high-resolution images of cells moving at velocities between 0.03 and 0.05 m/s with a spatial blur of no more than 500 nm (Figure S2B). Additionally, light sheet illumination was used to maximize excitation efficiencies by concentrating photons to a small volume, resulting in signal intensities one order of magnitude higher than when using standard epifluorescence excitation (Figures S2C and S2D). To ensure the efficient imaging of every single cell within a sample, the vertical dimension in the region of interest (ROI) was set to be slightly larger than the maximum diameter of a cell. As we are interested only in a narrow ROI along the focused excitation line (full width at half maximum [FWHM] of the Gaussian laser beam is 5 μm; Figure S2D), we were able to use this effect to increase the frame
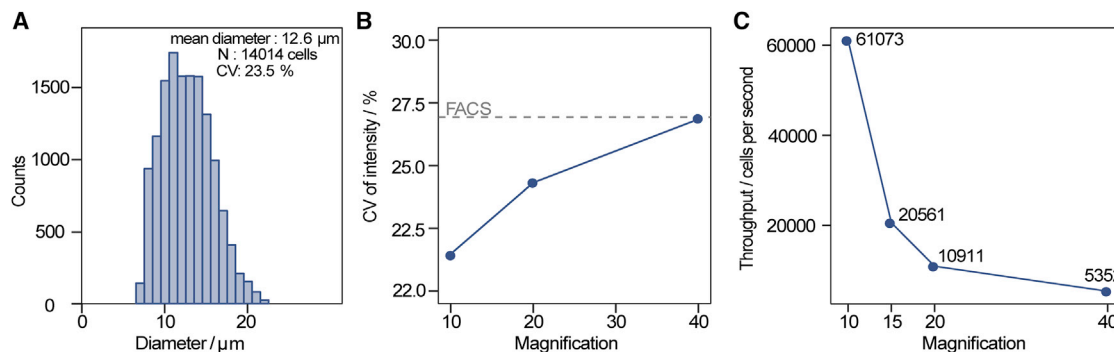
Figure 2. Performance of the imaging flow cytometer
(A) Size distribution of Jurkat cells stained with Alexa Fluor 488 WGA and imaged with a 10× 0.5 NA objective.
(B) Coefficient of variation for measured fluorescence intensities at three different magnifications: 10× 0.5 NA, 20× 0.5 NA, and 40× 0.75 NA. It should be noted that the CV for the 40× 0.75 NA objective is similar to that obtained when using a commercial FACS system (MoFlo Astrios EQ, Beckman Coulter), demonstrating that fluorescence variations are reduced when using a higher magnification objective.
(C) Variation in analytical throughput as a function of magnification. An experimental maximum throughput of 61,000 cells/s for fluorescence imaging was achieved when using a 10× 0.5 NA objective at a frame rate of 4,888 frames/s.

rate of the camera sensor. Values for the ROI, based on the magnification of the objectives used, are provided in the Table 1. The effective exposure time is defined by the length of the excitation pulses, with longer pulses resulting in higher signals but increased motion blur, as shown in Figure S2B. Using such an approach, we were able to probe the size and fluorescence of labeled Jurkat cells at extremely high throughput. As shown in Figure 2A, use of a 10× objective allows accurate assessment of the size of Jurkat cells (mean size 12.6 μm) fluorescently labeled with Alexa Fluor 488 wheat germ agglutinin (WGA). Significantly, the mean cell diameter of 12.6 μm calculated from Jurkat cells stained with Alexa Fluor 488 WGA (Figure 2A) is close to the 14.2 μm value obtained from blur-free bright-field images (Figure S3A) acquired from an analysis of a mixture of Jurkat and human B-lymphoid cells. The CVs in mean cell diameter extracted from fluorescence (23.5%) and bright-field (19.9%) measurements are also similar, confirming the precision of both imaging approaches in size determination. An additional important observation is that the CV decreases at higher magnifications, as size can be measured more accurately using high-magnification objective lenses (Figures S2E–S2H).

The measurement of the CV of fluorescence intensities at three different magnifications (10×, 20×, and 40×) highlights the accuracy in fluorescence quantification compared with a high-end commercial fluorescence-activated cell sorting (FACS) instrument (Astrios MoFlo, Beckman Coulter) operating at much lower throughput of 5,000 cells/s (Figure 2B). Indeed, the CV for the 40× 0.75 NA objective perfectly matches that obtained from the commercial instrument. We attribute the variation in fluorescence intensity to variations in staining, as the same cell sample yields an identical CV when analyzed with a FACS instrument, pre-calibrated with fluorescent beads. A measured maximum throughput of 61,000 cells/s was achieved when using a 10× 0.5 NA objective at a frame rate of 4,888 frames/s (Figure 2C). Using 15× magnification, the measured throughput was reduced to 20,561 cells/s because of the magnified field of view (and lower frame rate). Significantly, when using such a

magnification, sub-cellular localization of 1 μm cytoplasmic granules can be achieved at a much higher throughput than has been previously reported (Miura et al., 2018; Mikami et al., 2018). Even when using 20× magnification, the measured throughput (11,000 cells/s) and spatial resolution are 5 times higher and 2 times higher, respectively, than achievable with the Amnis ImageStream X when operating at 40× magnification. Indeed, the reported maximal throughput of the Amnis Image-Stream X flow cytometer assumes a much larger pixel size than in the present imaging flow cytometer and relatively dense cell spacing. When using a 1,331 × 90 μm ROI, the current platform is successful in accurate size analysis of a mixed population of Jurkat and human B-lymphoid cells (in a 1:1 ratio) at rates in excess of 400,000 cells/s (Figures S3B and S3C). Put simply, the present system can image enormous numbers of rapidly moving cells in an ultra-high-throughput manner with an imaging resolution defined by a 10× magnification objective.

The ability to resolve different fluorescent intensities and quantitatively measure low-fluorescence sub-populations is most commonly used to assess the analytical sensitivity of a flow cytometer. To this end, calibration was performed using MESF (molecules of equivalent soluble fluorophores) beads, yielding a detection sensitivity of 3,200 MESF units (Figures S4A–S4D) at 0.05 m/s and a throughput of 61,000 particles/s. By reducing the particle velocity and thus increasing the effective exposure time, detection sensitivity can be increased significantly, albeit at the expense of throughput (Figure S4E; Table S1). Additionally, adoption of a dual-view optical configuration allowed the implementation of a bright-field imaging modality for the concurrent investigation of cell morphology (Figures S4F–S4H).

Morphometric analysis of yeast and human cells
To evaluate the performance of the high-throughput imaging flow cytometer in quantifying subtle changes in sub-cellular structures, we analyzed the localization of stress granules and P/GW-bodies in yeast and human cells, respectively. Stress
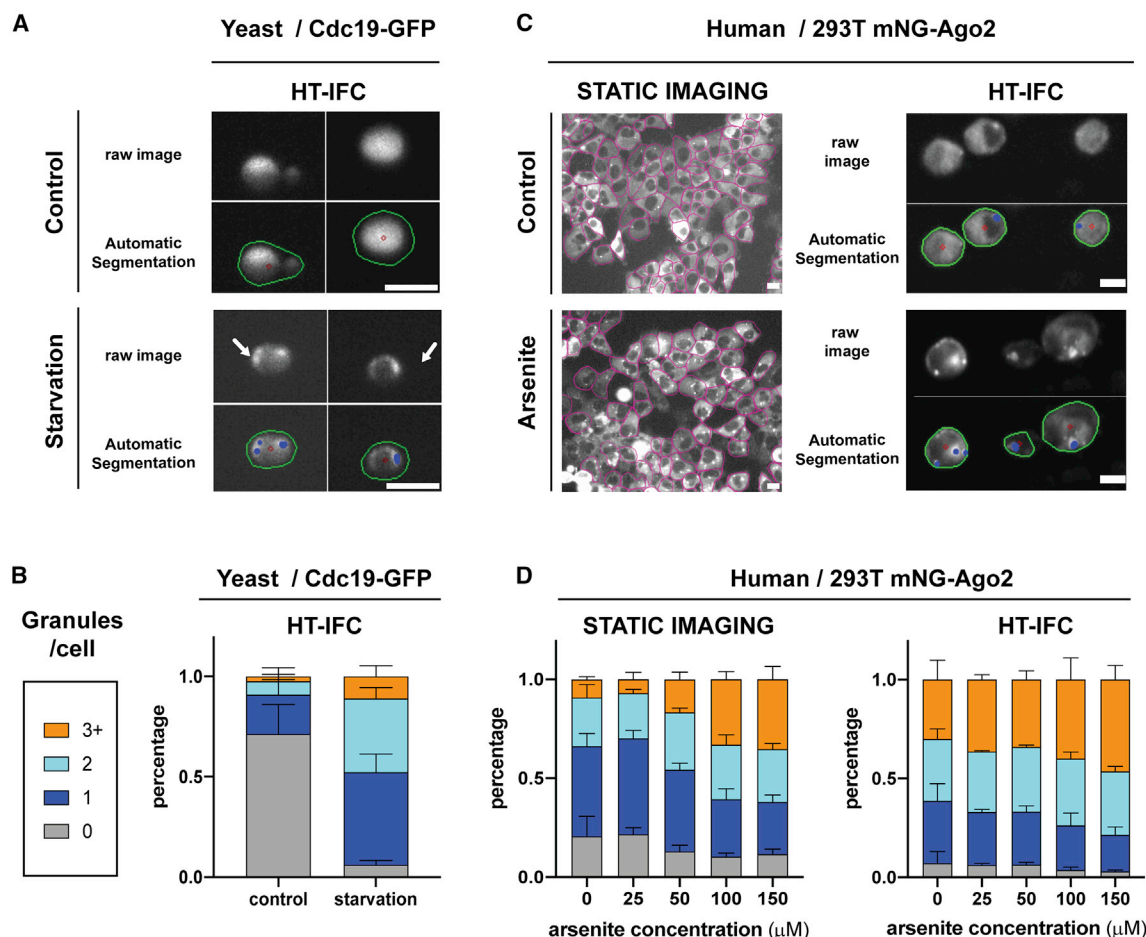
Figure 3. Variation in the number of P-bodies and stress granules in yeast cells and mammalian cells in response to external stimuli

(A) Flow cytometry images at 60× magnification of yeast growing within the exponential growth phase (control) and within the stationary phase (starvation). Scale bars, 5 μm.

(B) Percentage of yeast cells containing given numbers of aggregates, highlighting a clear difference between the control and starvation samples.

(C) Left: representative image at 20× magnification of adherent 293T expressing mNG-AGO2 under control and arsenite condition for static imaging. Within each image, cells were manually segmented (pink mask) for mNG-AGO2-positive cytoplasmic granule counting. Scale bars, 20 μm. Right: 293T cell images obtained in the imaging flow cytometer at 15× magnification are automatically segmented (green mask) and processed. Scale bars, 10 μm.

(D) Percentage of adherent 293T cells containing given numbers of granules as a function of arsenite concentration under static (left) and in-flow imaging conditions (right).

For (B) and (D), error bars represent the standard deviation.

granules are cytosolic structures that form within yeast cells in response to various stresses (such as starvation or oxidative stress) by phase separation and are thought to contribute to cellular adaptation by sequestering proteins and RNA to prevent their degradation and allowing the efficient restart of cell growth upon stress relief (Protter and Parker, 2016; Rabouille and Alberti, 2017; Buchan, 2014). On the other hand, P-bodies are small (500 nm to 1 μm in diameter) membrane-less cytoplasmic organelles in human cells that are intimately involved in RNA metabolism pathways, including RNA decay, stress-induced translational inhibition, and RNA silencing (Protter and Parker, 2016; Parker and Sheth, 2007).

Initially, we chose to study the localization of yeast pyruvate kinase, Cdc19, which aggregates in response to starvation and heat stress (Figures 3A and 3B) (Cereghetti et al., 2018; Saad et al., 2017). In line with previous experiments (Saad et al., 2017), analysis of images at 60× magnification indicated that Cdc19-GFP was found uniformly in the cytosol under control conditions but formed between one and two granules per cell during the stationary phase (48 h, long-term glucose starvation) (Figure 3B). On the basis of these images, we calculated the subcellular spatial resolution of our platform to be approximately 500 nm (Figure S5), a value essentially equivalent to that in static imaging (Cereghetti et al., 2018). We next investigated the subcellular localization of Argonaute 2 (AGO2), a protein from the RNA silencing pathway and P/GW-body constituents in human cells (Chen et al., 2009; Li et al., 2008). As previously reported (Leung and Sharp, 2013), 293T cells stably expressing fluorescently tagged AGO2 (mNeonGreen-AGO2) exhibit both a diffuse cytoplasmic emission pattern along with one to three granular
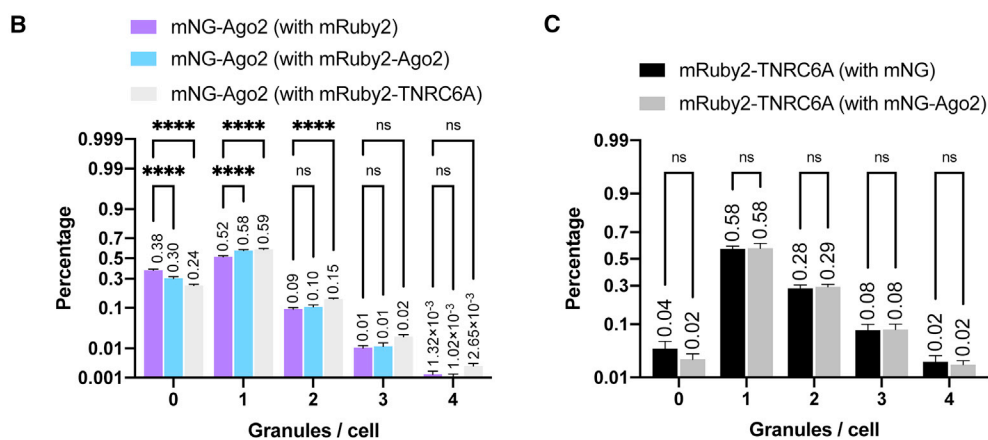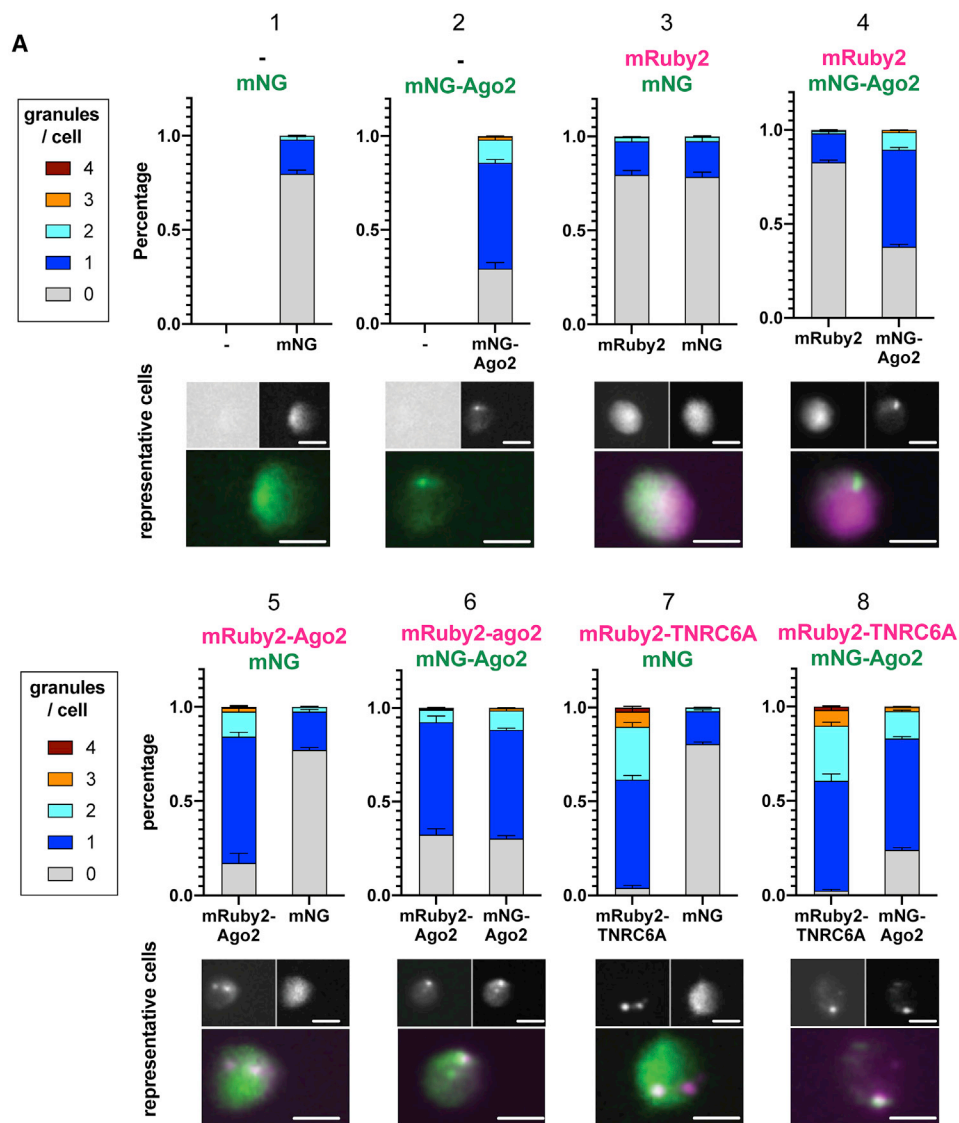
(legend on next page)

cytoplasmic structures per cell (characteristic of P/GW-bodies), features that are absent in control cells expressing only free mNeonGreen (mNG) (Figure 3C). Several stress-activated kinase pathways known to be activated in cancers (e.g., p38, AKT) directly control Argonaute shuttling and transfer into P/GW-bodies and stress granules by direct phosphorylation (Horman et al., 2013; Zeng et al., 2008). Among such stresses, oxidative stress induced by arsenite treatment has been previously shown to increase the number of AGO2-positive RNA granules in cells (Detzer et al., 2011). Indeed, treatment of cells with arsenite does lead to a dose-dependent increase in the number of mNG-AGO2-positive granules per cell, as detected by static fluorescence microscopy (Figures 3C and 3D, left panels) and by high-throughput IFC (Figures 3C and 3D, right panels). Here it should be noted that the different cell morphology (spherical versus flat cells) during image acquisition, as well as the image post-processing approaches (manual versus automatic segmentation and granule counting), may explain the different proportion of AGO2-positive granules per cell between the static imaging and imaging flow cytometry analyses. That said, it is evident that our approach, compared with static imaging, affords equivalent quantification of sub-micrometer, sub-cellular variations (Figure S5) in single mammalian cells but at dramatically improved throughput of 20,000 cells/s.

We also assessed the performance of our high-throughput IFC platform for dual-color co-localization assays in mammalian cells. We chose to investigate the sub-cellular localization of two RNA binding proteins; Trinucleotide Repeat-Containing Gene 6A protein (TNRC6A) and AGO2 in 293T cells. TNRC6A protein is a direct AGO2 interactor and has been shown to co-localize with mAGO2 within cytoplasmic RNA granules (Jakymiw et al., 2005). For this purpose, we co-expressed mRuby2-TNRC6A, mRuby2-AGO2, or free mRuby2 (as a control) in 293T cells stably expressing mNG-AGO2 or mNG (control samples) and performed co-localization analysis by quantifying the number of positive granular structures for each fluorescence channel (Figure 4) or the pixel intensity correlation in a large cell population (Figure 5).

Control experiments with 293T cells expressing mNG (Figure 4A, panels 1, 3, 5, and 7) and/or mRuby2 (Figure 4A, panels 3 and 4) show the expected characteristics of each protein fluorophore with around 80% of cells with no detectable foci. In sharp contrast, and as previously shown in Figure 3, mNG-AGO2 expressing cells exhibit one (56.4% of the cell population) or two (12.3%) cytoplasmic foci (Figure 4A, panel 2). mRuby2-AGO2 share a similar distribution with a cell population exhibiting one (67.1%) or two (13.2%) cytoplasmic foci (Figure 4A, panel 5). On the other hand, mRuby2-TNRC6A cells display a higher

proportion of cytoplasmic foci per cell (one [58.4%], two [28%], or three [7.9%]) than mRuby2- or mNG-tagged AGO2 (Figure 4A, panels 7 and 8). We demonstrate that in mNG-AGO2 cells, the number of granules per cell significantly increases with co-expression of mRuby2-AGO2 and mRuby2-TNRC6A, compared with co-expression of mRuby2 alone (Figure 4B). Importantly, although the change in mean percentages is modest (Figure 4B; 58% versus 52% for the one-granule category), it is associated with a highly significant p value (p < 0.000001), demonstrating that our IFC platform could indeed detect statistically significant and subtle sub-cellular localization changes (originating from distinct proteins) within a single cell, at high-spatial resolution and at a throughput of 20,000 cells/s, when using a 0.5 NA 15× objective. However, no significant change was observed in the distribution number of mRuby2-TNRC6A-positive granules when co-expressed in mNG-AGO2 or mNG cells (Figure 4C). Importantly, by quantification of granule co-localization percentage in individual cells, we show that mRuby2-TNRC6A, or mNG-AGO2, foci co-localize with mNG-AGO2 foci at much higher percentages (51.3% and 45.6%, respectively), than the control co-expressing the free fluorescent protein (13%–23%) (Figure S6). This confirms that both proteins associate with overlapping RNA granule compartments as previously reported (Nishi et al., 2013).

We then investigated whether images extracted from our imaging flow cytometer could be used to detect dual-color protein co-localization among a large cell population and under the aforementioned treatment conditions. Such a strategy, in principle, allows high-throughput quantification of the correlated spatial distribution (Aaron et al., 2018) of two distinct proteins via automatic image analysis and without prior knowledge of protein distribution over the population. We applied this strategy to mNG or mNG-AGO2 293T cells co-expressing mRuby2, mRuby2-AGO2, or mRuby2-TNRC6A (Figure 5). After high-throughput image acquisition using our IFC platform, we performed automatic segmentation and extracted intensities for each x-y pixel coordinate of each segmented cell image, from both green and red channels (Figure 5, left panel). We then computed the corresponding correlation coefficient for each cell, and plotted the R value distribution as violin plots for each condition, noting the median (Figure 5, right panel, red dashed line) and 25th and 75th percentile values (Figure 5, right panel, side lines). Such a representation highlights protein co-localization variability throughout the entire population (Figure 5, right panel). We also present a dual-channel image and corresponding two-dimensional histogram of red and green pixel intensities (including R and p values) for a representative cell under each condition. As expected from the prior analysis (Figure 4), we

Figure 4. Dual-color IFC for high-throughput co-localization studies
293T cells expressing mNG and mNG-AGO2 are transfected with different mRuby-tagged constructs.
(A) Granule counts for green and red channels, with the y axis representing percentages of fluorescently labeled cells. Cartoons illustrate representative localization states of the corresponding transfected cells. Small image panels show green (top) and red (bottom) channels, with an overlay of both channels being provided in the large image on the right-hand side. Scale bars, 10 μm. Error bars represent the standard deviation.
(B) Percentage of mNG-positive granules in mNG-AGO2 cells co-expressing mRuby2, mRuby2-AGO2, or mRuby2-TNRC6.
(C) Percentage of mRuby2-positive granules in mRuby2-TNRC6A cells co-expressing mNG or mNG-AGO2.
For (B) and (C) we represent statistically significant difference (ns, non-significant; *p ≤ 0.05, **p ≤ 0.01, ***p ≤ 0.001, and ****p ≤ 0.0001). All images were acquired at 20× magnification.
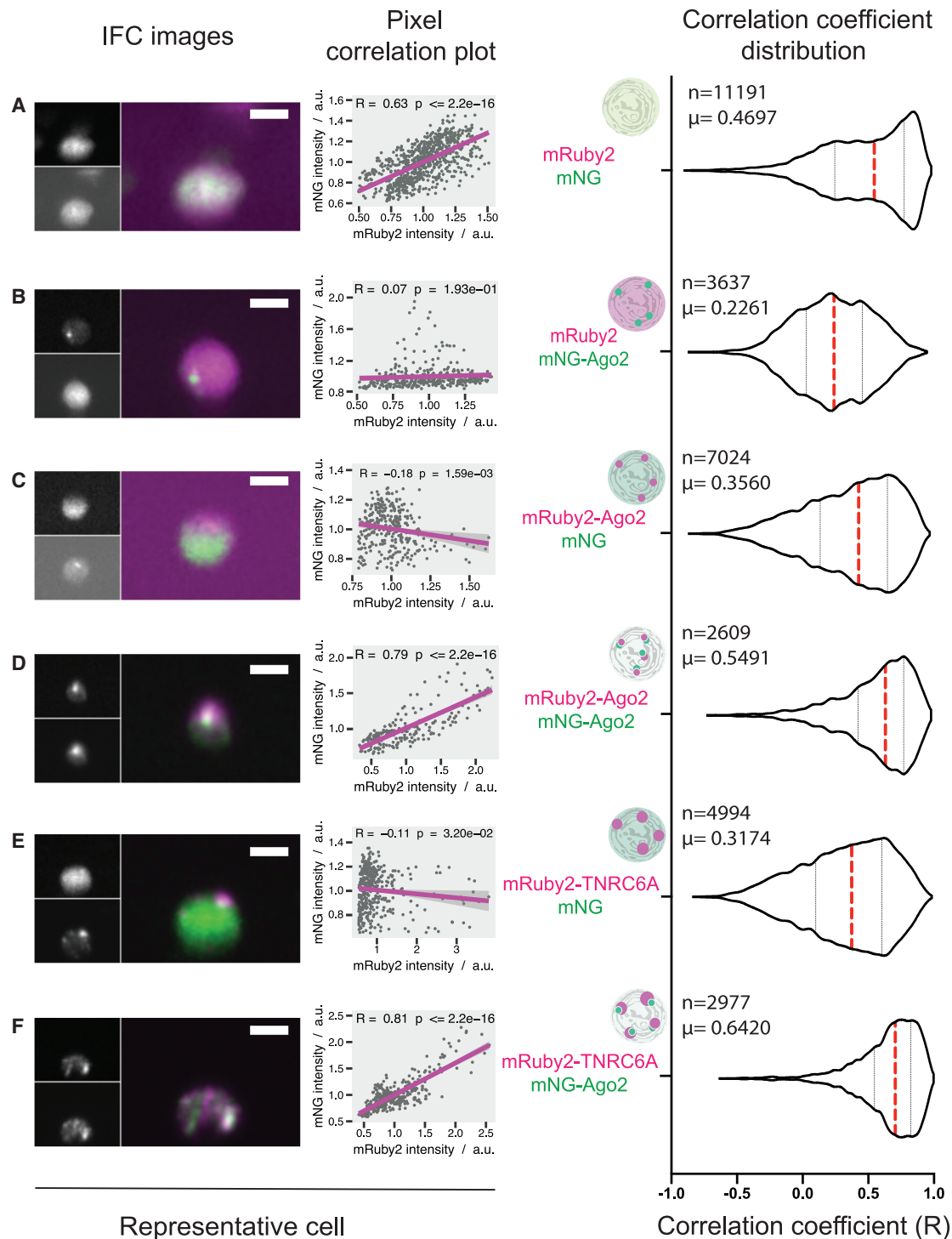
Figure 5. Co-localization plots for single-pixel intensities of normalized mNG and mRuby2 pixel intensities

(A–F) From left to right, (i) representative dual-color image, (ii) corresponding scatterplots of single-pixel intensities, (iii) distribution of correlation coefficient (R) between the two channel pixel intensity for the number of cells (n) investigated, and the median value indicated as dashed red line. The average (μ) correlation coefficient correlation value in each condition is reported in the graph as a means to quantify the degree of co-localization between fluorophores (Aaron et al., 2018). The pixel intensity for each cell was normalized to its average intensity value, with only the top 10% of the brightest pixels being retained for analysis. Scale bars, 10 μm. All images were acquired at 20× magnification.

observe an increased correlation coefficient distribution for cells co-expressing mRuby2-AGO2/mNG-AGO2 (Figure 5D) (R = 0.5391, n = 2,609) or mRuby2-TNRC6A/mNG-AGO2 (R = 0.6420, n = 2,977) (Figure 5F) compared with cells co-expressing mRuby2-AGO2/mNG (R = 0.3560, n = 7,024) (Figure 5C) or mRuby2-TNRC6/mNG (R = 0.3174, n = 4,994) (Figure 5E). Interestingly, and as a control, we observed a high-correlation coefficient for cells co-expressing mNG/mRuby2 (R = 0.4697, n = 11,191), as both monomeric fluorescent proteins are known to exhibit diffuse patterns throughout the whole cell (Figure 5A). It is worth mentioning that because of the extremely large number of analyzed cells, the analysis of variance (ANOVA) reports a statistically significant difference in the R value distribution between each experimental condition (Table S2). Accordingly, it is evident that the developed imaging flow cytometer is able to deliver high-quality images of single cells at high throughput, which in turn allows the quantification of subtle changes in the number and organization of small sub-cellular structure and the performance of co-localization studies on large number of cells.

DISCUSSION

We have presented an experimental platform for cellular analysis that successfully combines the power of optical microscopy in extracting morphological features at high resolution with the ability of conventional flow cytometry to rapidly screen large number of cells. As previously noted, the key reasons why imaging flow cytometers are normally unable to provide high-spatial resolution imaging at high throughput relate to motion blur, and thus a trade-off exists between analytical throughput and optical resolution. To address this limitation, we have adopted stroboscopic illumination to acquire high-resolution and blur-free images at ultra-high-throughput, which enables morphological characterization of cells within heterogeneous populations.

The resolving power of any camera-based imaging system depends sensitively on the sensor pixel size (Table 1). In the present system, a 6.5 μm pixel size combined with the adoption of a 10× objective yields an effective pixel size of 0.65 μm. A 40× objective results in an effective pixel size of 0.16 μm, and use of a 60× objective results in an effective pixel size of only 0.108 μm. In practice, the 40× objective is useful for mammalian cells because they fit well within the field of view (332 × 25 μm), while the 60× objective provides higher magnification for small species, such as yeast cells. On the basis of our measurements that relate cell velocity to motion blur (Figure S2B), the operating speed that provides for optimum throughput is approximately 0.05 m/s. Significantly, when combined with a 15× magnification objective, the imaging system provides for both high-throughput operation and high-resolution imaging (i.e., an effective pixel size of 0.43 μm). In this regard, it is interesting to note that magnification of 15× matches the pixel size of the best commercial imaging flow cytometer when using a 40× objective (Table 1). An analysis of experimentally measured imaging rates as well as resolution (determined by the objective) and the pixel size of the camera are provided in Table 1. At 40× magnification, the throughput of the gold-standard commercial imaging flow cytometer is approximately 2,000 cells/s. For the same pixel area conditions (Table 1), our stroboscopic imaging flow cytometer

provides an order of magnitude higher throughput (~20,000 cells/s) at 15× magnification. In this regard, it is important to note that although some previously reported imaging flow cytometers claim analytical throughput of 10,000 cells/s (Miura et al., 2018), these values originate from extrapolations based on the flow rate of hydrodynamic focusing and the frame rate of the camera. Because cells are not equally spaced and travel in a random order, the number of cells will not be constant for each frame and thus cannot be used to accurately predict throughput.

According to sampling theory, optimal spatial resolution is achieved when the pixel size of the camera sensor is half the diffraction-limited resolution of an optical system (Shannon, 1949). This is commonly termed the Nyquist limit and determines the maximum acceptable pixel size needed to meet the optical resolution of a specific objective. To fulfil the Nyquist criterion, the size of the object of interest (such as a stress granule or P-body) inside a cell should be between 500 nm and 1 μm in size. Accordingly, to resolve an object 700 nm in size (the lower boundary for stress granules and P-bodies), an objective with a 20× magnification and NA of 0.5 is required (Table 1). At this magnification, the projected image will be 13.5 μm, and thus a camera with a pixel size of 6.7 μm (13.5/2) or smaller is necessary. Significantly, this value matches perfectly with the objective type and complementary metal oxide semiconductor (CMOS) camera pixel size used in the current platform. This is an important parameter when quantifying sub-cellular distributions of stress granules, for example, those associated with certain functions of the SAM domain and HD domain containing protein 1 (SAMHD1) (Hu et al., 2015), and in the localization of stress granules of several inhibitory immune checkpoint mRNAs (Franchini et al., 2019).

Such localization-based applications are typically accomplished using conventional static (and low-throughput) imaging approaches, since intensity-based measurements are unable to provide concurrent information on protein localization of 1 μm foci. In contrast, our platform may be used for efficient and reliable foci counting in radiation-damaged cells (Ivashkevich et al., 2012) at a throughput two to three orders of magnitude higher than currently possible. Additionally, the use of conventional microscopy and manual cell counting in clinical blood analysis is both labor intensive and low throughput. Adoption of our cytometry platform for such task would allow quantification of physiological and immunological function, again at a throughput two to three orders of magnitude higher than currently possible.

As we have stressed, a lack of image information is the major limitation of conventional flow cytometers, and thus platforms that combine the high-throughput nature of conventional flow cytometry with the high-resolution imaging features of an optical microscope are extremely powerful. This is confirmed by our high-throughput imaging of fluorescent RNA granules in flow, with a spatial resolution close to the diffraction limit (Figure S5A). The use of stroboscopic illumination to prevent motion blur is highly effective but is characterized by a trade-off between sensitivity and laser strobe duration (i.e., decreasing the strobe pulse duration minimizes motion blur but also reduces sensitivity). However, there is a trade-off between sensitivity and throughput, as high-speed imaging requires shorter exposure

durations to obtain blur-free images. Issues related to motion blur (and thus sensitivity) can also be circumvented to a large degree by microfluidic-based fluid manipulations, which enable efficient positioning of cells at low average velocities. In this respect, we have demonstrated the utility of viscoelastic carrier fluids within wide microfluidic channels for precise lateral and axial positioning of cells at low volumetric flow rates. Indeed, it should not be forgotten that such a simple and robust method for focusing cells could be easily be implemented within a portable flow cytometry platform, removing the need for excessive volumes of sheath fluid.

Conventional flow cytometers are ill equipped to handle small-volume clinical samples. Indeed, without an integrated micro-scale fluid actuation system, it is challenging to manipulate small sample volumes without causing appreciable cell damage. Existing flow cytometry approaches allow high-throughput analysis of the phenotypic characteristics of a cell population but typically require many more cells than exist within a single embryoid body (approximately 10^4 cells) (Wilson et al., 2014). Put simply, there is no existing method that can easily quantify the phenotypic diversity of single embryoid bodies. Moreover, analysis of small numbers of precious cells is critical when probing cellular samples from clinical biopsies. For example, when studying lymphocyte activation in clinical samples (Hritzo et al., 2018), quantitative information on protein localization is highly desirable. In this respect, the presented IFC platform is capable of efficiently loading small (microliter-sized) sample volumes containing only a few hundred cells.

More generally, we note that the present imaging cytometry platform integrated with artificial intelligence-aided image processing would allow multiparametric quantification of cell populations with unrivaled throughput and resolution and facilitate the identification of cell characteristics relevant for sample classification in a range of molecular diagnostic strategies, such as morphology-based diagnosis of rare cells in blood diseases (Brereton et al., 2015; Bigorra et al., 2019) or circulating tumor cells (Ogle et al., 2016). In addition, our platform is ideally suited for the classification of membrane-less organelles on the basis of their localization and composition inside cells. Such a capability is critical, for example, in the detection of protein aggregation associated with a range of neurodegenerative diseases (Wolozin and Ivanov, 2019; Fan and Leung, 2016). Moreover, the platform could be integrated with refractive microlens arrays, with a view to significantly enhancing analytical throughput in wide-field imaging applications (Holzner et al., 2018). In this regard, an obvious application would be in CRISPR-based genetic screening for the identification of protein candidates that affect stress granule assembly (Wheeler et al., 2020).

Herein we have also addressed the co-localization of two fluorescently labeled proteins in live cells using two independent methods. In the first one, we analyzed the percentage of granules occupying the same spot in both mNG and mRuby2 channels (Figure S6). This involves initially determining the position of high-intensity "spots" in cells and then testing whether spot locations from both channels overlap. This approach is useful when analyzing sub-cellular structures such as RNA granules. In a second approach, we calculated the correlation factor (R) of pixel intensities between both channels to estimate co-localization at the whole-cell level (Figure 5). This approach tests whether the overall sub-cellular distribution of two proteins overlaps, suggesting a functional interaction or association within similar organelles. In these analyses, we used ANOVA to test whether there was a statistically significant change in the R value distribution from each cell across each co-expression condition. Because of the high-statistical power of such an analysis on thousands of cells, we demonstrate statistically significant differences for each pairwise comparison, thereby establishing the power of our high-throughput IFC approach. However, one needs to apply a different strategy for hit discovery during a screen (e.g., impact of a drug collection on Protein X and Y co-localization, protein interaction screening). Using a "spot" co-localization percentage (method 1), or correlation coefficient (method 2), one could establish a threshold for positive hits on the basis of positive control experiments using conditions (e.g., drug interactions) known to have positive impact on the co-localization events. Adequate negative controls are also needed to establish a baseline for background interaction. For example, Figures 5D and 5F clearly show that the mean correlation factor is above 0.5 only for the two conditions that are supposed to be positive for co-localization. Alternatively, one could perform a statistical test among biological replicates to identify a statistically significant change in the "spot" co-localization percentage (method 1) or correlation coefficient (method 2) compared with a reference condition (e.g., mock-treated cells versus drug-treated cells). Finally, one could apply a supervised or unsupervised machine learning image algorithm to classify the testing conditions. This last possibility is facilitated by the large samples engendered by high-throughput IFC and represents an exciting discovery approach.

Despite the efficacy of the present platform for high-throughput cellular imaging, the addition of a high-power light source (modulated at higher frequencies) and a high-quantum efficiency camera would enable blur-free imaging at even higher throughputs and with enhanced sensitivity. Despite these proposed improvements, our studies demonstrate the sensitivity of our cytometry platform for imaging cells at ultra-high throughput and screening large and heterogeneous cellular populations. To conclude, we have presented a microfluidic platform for high-resolution, high-throughput IFC, which incorporates a viscoelastic carrier fluid and stroboscopic laser light sheet illumination. Critically, the adoption of a wide-channel microfluidic format facilitates simple fluidic operation and greatly simplifies the optical detection scheme. As shown, such advances provide for an increase in analytical throughput of several orders of magnitude compared with existing imaging flow cytometers. Finally, it should also be noted that as contemporary cameras and computational tools become both faster and cheaper, the combination of our approach with "real-time" image analysis will have significant implications in a range of diagnostic applications.

STAR★METHODS

Detailed methods are provided in the online version of this paper and include the following:

- KEY RESOURCES TABLE

AUTHOR CONTRIBUTIONS

A.dM., S.S., and G.H. conceived the project and devised the research plan. S.S. and G.H. developed the instrumental platform and methodology and performed all experiments. G.H. and B.M. performed image processing and data analysis. B.M., D.v.L., G.C., and R.D. developed the cell protocols and cultured the biological samples. A.dM., S.S., and B.M. wrote the manuscript.

DECLARATION OF INTERESTS

The authors declare no competing interests.

REFERENCES

Aaron, J.S., Taylor, A.B., and Chew, T.L. (2018). Image co-localization—co-occurrence versus correlation. J. Cell Sci. *131*, 131–140.

Armbruster, D.A., and Pry, T. (2008). Limit of blank, limit of detection and limit of quantitation. Clin. Biochem. Rev. *29* (Suppl 1), S49–S52.

Barteneva, N.S., Fasler-Kan, E., and Vorobjev, I.A. (2012). Imaging flow cytometry: coping with heterogeneity in biological systems. J. Histochem. Cytochem. *60*, 723–733.

Basiji, D.A., Ortyn, W.E., Liang, L., Venkatachalam, V., and Morrissey, P. (2007). Cellular image analysis and imaging by flow cytometry. Clin. Lab. Med. *27*, 653–670, viii.

Berchtold, D., Battich, N., and Pelkmans, L. (2018). A systems-level study reveals regulators of membrane-less organelles in human cells. Mol. Cell *72*, 1035–1049.e5.

Bigorra, L., Larriba, I., and Gutiérrez-Gallego, R. (2019). Machine learning algorithms for accurate differential diagnosis of lymphocytosis based on cell population data. Br. J. Haematol. *184*, 1035–1037.

Boraldi, F., Bartolomeo, A., De Biasi, S., Orlando, S., Costa, S., Cossarizza, A., and Quaglino, D. (2016). Innovative flow cytometry allows accurate identification of rare circulating cells involved in endothelial dysfunction. PLoS ONE *11*, e0160153.

Brereton, M., De La Salle, B., Ardern, J., Hyde, K., and Burthem, J. (2015). Do we know why we make errors in morphological diagnosis? An analysis of approach and decision-making in haematological morphology. EBioMedicine *2*, 1224–1234.

Buchan, J.R. (2014). mRNP granules. Assembly, function, and connections with disease. RNA Biol. *11*, 1019–1030.

Cereghetti, G., Saad, S., Dechant, R., and Peter, M. (2018). Reversible, functional amyloids: towards an understanding of their regulation in yeast and humans. Cell Cycle *17*, 1545–1558.

Chen, C.Y.A., Zheng, D., Xia, Z., and Shyu, A.B. (2009). Ago-TNRC6 triggers microRNA-mediated decay by promoting two deadenylation steps. Nat. Struct. Mol. Biol. *16*, 1160–1166.

Crocker, J.C., and Grier, D.G. (1996). Methods of digital video microscopy for colloidal studies. J. Colloid Interface Sci. *179*, 298–310.

Detzer, A., Engel, C., Wünsche, W., and Sczakiel, G. (2011). Cell stress is related to re-localization of Argonaute 2 and to decreased RNA interference in human cells. Nucleic Acids Res. *39*, 2727–2741.

Di Carlo, D., Irimia, D., Tompkins, R.G., and Toner, M. (2007). Continuous inertial focusing, ordering, and separation of particles in microchannels. Proc. Natl. Acad. Sci. U S A *104*, 18892–18897.

Fan, A.C., and Leung, A.K.L. (2016). RNA granules and diseases: a case study of stress granules in ALS and FTLD. In RNA Processing: Disease and Genome-wide Probing, G.W. Yeo, ed. (Cham, Switzerland: Springer International Publishing), pp. 263–296.

Franchini, D.-M., Lanvin, O., Tosolini, M., Patras de Campaigno, E., Cammas, A., Péricart, S., Scarlata, C.-M., Lebras, M., Rossi, C., Ligat, L., et al. (2019). Microtubule-driven stress granule dynamics regulate inhibitory immune checkpoint expression in T cells. Cell Rep. *26*, 94–107.e7.

Gauthier, D.J., Sobota, J.A., Ferraro, F., Mains, R.E., and Lazure, C. (2008). Flow cytometry-assisted purification and proteomic analysis of the cortico-tropes dense-core secretory granules. Proteomics *8*, 3848–3861.

Goda, K., Ayazi, A., Gossett, D.R., Sadasivam, J., Lonappan, C.K., Sollier, E., Fard, A.M., Hur, S.C., Adam, J., Murray, C., et al. (2012). High-throughput single-microparticle imaging flow analyzer. Proc. Natl. Acad. Sci. U S A *109*, 11630–11635.

Grimwade, L.F., Fuller, K.A., and Erber, W.N. (2017). Applications of imaging flow cytometry in the diagnostic assessment of acute leukaemia. Methods *112*, 39–45.

Han, Y., and Lo, Y.H. (2015). Imaging cells in flow cytometer using spatial-temporal transformation. Sci. Rep. *5*, 13267.

Hasegawa, D., Bugarin, C., Giordan, M., Bresolin, S., Longoni, D., Micalizzi, C., Ramenghi, U., Bertaina, A., Basso, G., Locatelli, F., et al. (2013). Validation of flow cytometric phospho-STAT5 as a diagnostic tool for juvenile myelomonocytic leukemia. Blood Cancer J. *3*, e160.

Holzner, G., Stavrakis, S., and deMello, A. (2017). Elasto-inertial focusing of mammalian cells and bacteria using low molecular, low viscosity PEO solutions. Anal. Chem. *89*, 11653–11663.

Holzner, G., Du, Y., Cao, X., Choo, J., J deMello, A., and Stavrakis, S. (2018). An optofluidic system with integrated microlens arrays for parallel imaging flow cytometry. Lab Chip *18*, 3631–3637.

Horman, S.R., Janas, M.M., Litterst, C., Wang, B., MacRae, I.J., Sever, M.J., Morrissey, D.V., Graves, P., Luo, B., Umesalma, S., et al. (2013). Akt-mediated

phosphorylation of argonaute 2 downregulates cleavage and upregulates translational repression of MicroRNA targets. Mol. Cell *50*, 356–367.

Hritzo, M.K., Courneya, J.P., and Golding, A. (2018). Imaging flow cytometry: A method for examining dynamic native FOXO1 localization in human lymphocytes. J. Immunol. Methods *454*, 59–70.

Hu, S., Li, J., Xu, F., Mei, S., Le Duff, Y., Yin, L., Pang, X., Cen, S., Jin, Q., Liang, C., and Guo, F. (2015). SAMHD1 inhibits LINE-1 retrotransposition by promoting stress granule formation. PLoS Genet. *11*, e1005367.

Hui, Y.Y., Su, L.-J., Chen, O.Y., Chen, Y.-T., Liu, T.-M., and Chang, H.-C. (2014). Wide-field imaging and flow cytometric analysis of cancer cells in blood by fluorescent nanodiamond labeling and time gating. Sci. Rep. *4*, 5574.

Ivashkevich, A., Redon, C.E., Nakamura, A.J., Martin, R.F., and Martin, O.A. (2012). Use of the γ-H2AX assay to monitor DNA damage and repair in translational cancer research. Cancer Lett. *327*, 123–133.

Jakymiw, A., Lian, S., Eystathioy, T., Li, S., Satoh, M., Hamel, J.C., Fritzler, M.J., and Chan, E.K.L. (2005). Disruption of GW bodies impairs mammalian RNA interference. Nat. Cell Biol. *7*, 1267–1274.

Leung, A.K.L., and Sharp, P.A. (2013). Quantifying Argonaute proteins in and out of GW/P-bodies: implications in microRNA activities. Adv. Exp. Med. Biol. *768*, 165–182.

Li, S., Lian, S.L., Moser, J.J., Fritzler, M.L., Fritzler, M.J., Satoh, M., and Chan, E.K. (2008). Identification of GW182 and its novel isoform TNGW1 as translational repressors in Ago2-mediated silencing. J. Cell Sci. *121*, 4134–4144.

López-Riquelme, N., Minguela, A., Villar-Permuy, F., Ciprian, D., Castillejo, A., Álvarez-López, M.-R., and Soto, J.-L. (2013). Imaging cytometry for counting circulating tumor cells: comparative analysis of the CellSearch vs Image-Stream systems. APMIS *121*, 1139–1143.

Mikami, H., Harmon, J., Kobayashi, H., Hamad, S., Wang, Y.S., Iwata, O., Suzuki, K., Ito, T., Aisaka, Y., Kutsuna, N., et al. (2018). Ultrafast confocal fluorescence microscopy beyond the fluorescence lifetime limit. Optica *5*, 117–126.

Mikami, H., Kawaguchi, M., Huang, C.-J., Matsumura, H., Sugimura, T., Huang, K., Lei, C., Ueno, S., Miura, T., Ito, T., et al. (2020). Virtual-freezing fluorescence imaging flow cytometry. Nat. Commun. *11*, 1162.

Miura, T., Mikami, H., Isozaki, A., Ito, T., Ozeki, Y., and Goda, K. (2018). On-chip light-sheet fluorescence imaging flow cytometry at a high flow speed of 1 m/s. Biomed. Opt. Express *9*, 3424–3433.

Nishi, K., Nishi, A., Nagasawa, T., and Ui-Tei, K. (2013). Human TNRC6A is an Argonaute-navigator protein for microRNA-mediated gene silencing in the nucleus. RNA *19*, 17–35.

Nitta, N., Sugimura, T., Isozaki, A., Mikami, H., Hiraki, K., Sakuma, S., Iino, T., Arai, F., Endo, T., Fujiwaki, Y., et al. (2018). Intelligent image-activated cell sorting. Cell *175*, 266–276.e13.

Ogle, L.F., Orr, J.G., Willoughby, C.E., Hutton, C., McPherson, S., Plummer, R., Boddy, A.V., Curtin, N.J., Jamieson, D., and Reeves, H.L. (2016). Image-stream detection and characterisation of circulating tumour cells—a liquid biopsy for hepatocellular carcinoma? J. Hepatol. *65*, 305–313.

Parker, R., and Sheth, U. (2007). P bodies and the control of mRNA translation and degradation. Mol. Cell *25*, 635–646.

Protter, D.S.W., and Parker, R. (2016). Principles and properties of stress granules. Trends Cell Biol. *26*, 668–679.

Rabouille, C., and Alberti, S. (2017). Cell adaptation upon stress: the emerging role of membrane-less compartments. Curr. Opin. Cell Biol. *47*, 34–42.

Rane, A.S., Rutkauskaite, J., deMello, A., and Stavrakis, S. (2017). High-throughput multi-parametric imaging flow cytometry. Chem *3*, 588–602.

Saad, S., Cereghetti, G., Feng, Y., Picotti, P., Peter, M., and Dechant, R. (2017). Reversible protein aggregation is a protective mechanism to ensure cell cycle restart after stress. Nat. Cell Biol. *19*, 1202–1213.

Shannon, C.E. (1949). Communication in the presence of noise. Proc. IEEE *37*, 10–21.

van Beers, E.J., Samsel, L., Mendelsohn, L., Saiyed, R., Fertrin, K.Y., Brantner, C.A., Daniels, M.P., Nichols, J., McCoy, J.P., and Kato, G.J. (2014). Imaging flow cytometry for automated detection of hypoxia-induced erythrocyte shape change in sickle cell disease. Am. J. Hematol. *89*, 598–603.

Wang, L., Gaigalas, A.K., Abbasi, F., Marti, G.E., Vogt, R.F., and Schwartz, A. (2002). Quantitating fluorescence intensity from fluorophores: practical use of MESF values. J. Res. Natl. Inst. Stand. Technol. *107*, 339–353.

Wheeler, E.C., Vu, A.Q., Einstein, J.M., DiSalvo, M., Ahmed, N., Van Nostrand, E.L., Shishkin, A.A., Jin, W., Allbritton, N.L., and Yeo, G.W. (2020). Pooled CRISPR screens with imaging on microraft arrays reveals stress granule-regulatory factors. Nat. Methods *17*, 636–642.

Wilson, J.L., Suri, S., Singh, A., Rivet, C.A., Lu, H., and McDevitt, T.C. (2014). Single-cell analysis of embryoid body heterogeneity using microfluidic trapping array. Biomed. Microdevices *16*, 79–90.

Wolozin, B., and Ivanov, P. (2019). Stress granules and neurodegeneration. Nat. Rev. Neurosci. *20*, 649–666.

Wu, J.L., Xu, Y.Q., Xu, J.J., Wei, X.M., Chan, A.C.S., Tang, A.H.L., Lau, A.K.S., Chung, B.M.F., Cheung Shum, H., Lam, E.Y., et al. (2017). Ultrafast laser-scanning time-stretch imaging at visible wavelengths. Light Sci. Appl. *6*, e16196.

Zeng, Y., Sankala, H., Zhang, X., and Graves, P.R. (2008). Phosphorylation of Argonaute 2 at serine-387 facilitates its localization to processing bodies. Biochem. J. *413*, 429–436.

STAR★METHODS

KEY RESOURCES TABLE

REAGENT or RESOURCE	SOURCE	IDENTIFIER
Chemicals, peptides, and recombinant proteins		
Quantum Alexa Fluor 488 MESF	Bangs Laboratories	Cat#488
RPMI-1640	Thermo Scientific	Cat#11875101
Premium Fetal bovine Serum	Thermo Scientific	Cat#A4766
Penicillin-Streptomycin (10,000 U/mL)	Thermo Scientific	Cat#15140148
Alexa Fluor 488 WGA	Thermo Scientific	Cat#A12379
Pluronic ® F-127	Sigma-Aldrich	Cat#P2443-250G
DMEM, High Glucose, GlutaMAX, HEPES	Thermo Scientific	Cat#32430100
PEImax	Polysciences Europe	Cat#24765-1
Sodium Arsenite	Sigma-Aldrich	Cat#S7400
Poly(ethylene oxide)	Sigma-Aldrich	Cat#372781-5G
polydimethoxysilane (PDMS)	Dow Corning	Cat#Sylgard 184
doxycycline hyclate	Sigma-Aldrich	*Cat#D9891*
PBS pH 7.4	Thermo Scientific	Cat#10010056
Paraformaldehyde	Sigma-Aldrich	Cat#P6148
OptiPrep Density Gradient Medium	Sigma-Aldrich	Cat#D1556
HBSS, no calcium, no magnesium, no phenol red	Thermo Scientific	Cat#14175079
Experimental models: cell lines		
JURKAT Clone E6-1	ATCC	Cat#TIB-152
Human B-lymphoid	Amanda G. Fisher (Imperial College)	N/A
Flp-In T-REx 293	Thermo Scientific	Cat#R78007
Flp-In T-REx 293 mNG	B. Mateescu (University Zurich)	N/A
Flp-In T-REx 293 mNG-Ago2	B. Mateescu (University Zurich)	N/A
ySS12 (genotype BY4741, *CDC19::CDC19-GFP-HIS3)*	Thermo Scientific, Dechant lab (ETHZ)	Yeast-GFP Clone Collection
Recombinant DNA		
pcDNA5/FRT/TO-mRuby2-TNRC6A	B. Mateescu (University Zurich)	N/A
pcDNA5/FRT/TO	Thermo Scientific	Cat#V652020
pcDNA5/FRT/TO-mRuby2	B. Mateescu (University Zurich)	N/A
pcDNA5/FRT/TO-mRuby2-Ago2	B. Mateescu (University Zurich)	N/A
Software and algorithms		
Prism	Graphpad	https://www.graphpad.com/scientific-software/prism/
AutoCAD	Autodesk	https://www.autodesk.com/products/autocad/overview?term=1-YEAR&support=null
R	www.r-project.org	https://www.r-project.org/
COMSOL Multiphysics 5.4	COMSOL	http://cn.comsol.com/comsol-multiphysics
Other		
Beamsplitter HC BS 560	AHF	Cat#F38-560
520/35 BrightLine HC	AHF	Cat#F37-520
590 LP ET Longpass Filter	AHF	Cat#F47-591
Acoustooptical tunable filter	AA Opto-electronic	Cat#AOTF nC-400-650-TN
Cylindrical lens	Thorlabs	Cat#LJ1558RM-A
Acylindrical lens	Thorlabs	Cat#AYL2520-A

RESOURCE AVAILABILITY

Lead contact
Further information and requests for resources should be directed to and will be fulfilled by the Lead Contact, Andrew deMello (andrew.demello@chem.ethz.ch).

Materials availability
This study did not generate new unique reagents.

Data and code availability
The code supporting the current study has not been deposited in a public repository but is available from the corresponding author on request.

EXPERIMENTAL MODEL AND SUBJECT DETAILS

Cell culture, transfection and fixation
Experiments were performed on four different cell lines: JURKAT Clone E6-1 (LGC Standards GmbH, Wesel, Germany USA), Human B-lymphoid, 293T Flp-in T-REX (Life Technologies, Zug, Switzerland) and yeast. Jurkat and Human B-lymphoid cell lines were initially tested for mycoplasma contamination and then cultured in RPMI-1640 medium (Life Technologies, Zug, Switzerland) supplemented with 10% (v/v) FBS (Life Technologies, Zug Switzerland) and 1% (v/v) Penicillin-Streptomycin (10,000 U/mL, Life Technologies, Zug Switzerland) in a CO_2 incubator (New Brunswick Galaxy® 170 S, Eppendorf, Schönenbuch Switzerland) at 37°C, 5% CO_2, according to standard protocols. All experiments were performed on cells in the exponential (log) phase of growth. Cells were fixed in 4% para-formaldehyde for 10 minutes at room temperature, rinsed 3 times in HBSS buffer and incubated with Alexa Fluor 488 WGA (1:200, A12379, Life Technologies, Zug, Switzerland) for 10 minutes at room temperature. After rinsing twice with HBSS, cells were transferred in PBS and mixed with OptiPrep ® Density Gradient Medium (Sigma-Aldrich, Buchs, Switzerland) and the PEO solution to the desired ratio and used directly.

293T Flp-in T-REX cells expressing mNG or mNG-AGO2 cells were cultured in DMEM medium (Life Technologies, Zug, Switzerland), supplemented with Glutamax and HEPES (Life Technologies, Zug, Switzerland), and 10% fetal bovine serum (FBS, Life Technologies, Zug, Switzerland). It should be noted that our mNG tags also have a 3xFlag and SBP affinity peptide sequence at the N-terminal. Two days before analysis, 8 million cells were seeded in a 10 cm plate in the presence of doxycycline (2 μg/ml) to induce expression of the tagged protein. Transfection of the plasmid was performed using PEImax (Polysciences Europe GmbH, Hirschberg an der Bergstrasse, Germany), by mixing 180 μl of PEImax (1 mg/ml) with 9 μg of plasmid 24 hours after seeding, and replacing the medium after 8 hours. Then, 48 hours after plating, cells were treated with sodium arsenite (Sigma-Aldrich, Buchs Switzerland) for 2 hours. The medium was subsequently replaced with PBS buffer before 8-10 representative images (green, red and phase contrast) for each condition were acquired on a Floid fluorescence microscope (Life Technologies, Zug, Switzerland). Afterward, adherent cells were trypsinized, and the corresponding cell suspension washed once in PBS, before fixation in 2% paraformaldehyde for 10 minutes. Finally, the cell suspension was washed twice with PBS before re-suspending in DMEM supplemented with 10% FBS, and then washed with PBS.

Yeast media and growth conditions of cells were as described previously (Saad et al., 2017). Briefly, saturated overnight cultures were diluted into fresh synthetic complete media containing 2% glucose for 5 hours (mid-exponential phase), or for an additional 48 hours to ensure entry into the stationary phase (starvation). Cells were fixed using a 3.7% formaldehyde solution and incubated at room temperature for 10 minutes. Cells were washed twice in PBS by centrifugation and then imaged. The yeast strain used in the current experiments was ySS12 (Saad et al., 2017) (genotype: BY4741, CDC19::CDC19-GFP-HIS3, Life Technologies, Zug, Switzerland).

METHOD DETAILS

Microfluidic device fabrication
Microfluidic devices were fabricated using standard soft-lithographic techniques. Briefly, the two-dimensional channel pattern was designed using AutoCAD (AutoCAD 2017, Autodesk, San Rafael CA, USA) and printed onto a transparent film photomask (Micro Lithography Services Ltd, Chelmsford, United Kingdom). The photomask was subsequently used to pattern an SU-8-coated silicon wafer (Microchem Corporation, Westborough, USA) using conventional photolithography. A 10:1 mixture of polydimethoxysilane (PDMS) monomer and curing agent (Sylgard 184, Dow Corning, Midland, USA) was poured over the master-mold and peeled off after polymerization at 70°C for 4 hours. Inlet and outlet ports were created using a hole-puncher (Technical Innovations, West Palm Beach, USA) and the structured PDMS substrate then bonded to a planar glass substrate (Menzel-Glaser, Braunschweig, Germany) after exposing both surfaces to an oxygen plasma (EMITECH K1000X, Quorum Technologies, East Sussex, United Kingdom) for 60 s.

Microfluidic device structure

A schematic of the microfluidic device, comprising a single high aspect ratio channel, is shown in Figure 1B. Channel cross-sections were 59 × 665 μm (for experiments using a 20X objective), 59 × 1331 μm (for experiments using a 10X objective) and 38 × 332 μm for experiments using yeast cells. These dimensions guaranteed an even distribution of cells across the channel, as shown in Figure S1. The height of the microfluidic channel was set to 59 μm, so as to satisfy the blockage ratio criterion, $\beta = a/h$, (where a and h are the cell diameter and the characteristic height of the microchannel) to be smaller than 0.25. The average diameter of the mammalian cells used in this study was 13 μm and the average diameter of yeast cells is approximately 4 μm. Such conditions yielded single file/in plane focusing of cells according to previous studies (Holzner et al., 2017). Computational fluid dynamics simulations of the flow distribution across the microfluidic chip were performed in COMSOL Multiphysics 5.4,

Device operation

PDMS devices were initially rinsed in water and then incubated for 10 minutes in a 2% w/w Pluronic ® F-127 (Sigma-Aldrich, Buchs, Switzerland) solution to prevent cells sticking to the channel walls. The cell suspension (at concentrations up to 25 million cells per mL) was loaded into a 1 mL syringe (Hamilton Laboratory Products, NV, USA) and delivered at the desired flow rate using a precision syringe pump (neMESYS, Cetoni, Korbussen, Germany). The microfluidic device was placed on a motorized *xy* translation stage (Mad City Laboratories, Maddison, USA) mounted on an inverted Ti-E microscope (Nikon, Zurich, Switzerland). In all experiments, cells and beads were suspended in a viscoelastic polyethylene oxide solution (PEO) solution to allow for elasto inertial focusing. Multiple parameters must be controlled to ensure efficient focusing cells into a single file. These include the molecular weight of the polymer, concentration of the polymer solution, microfluidic channel geometry, the blockage ratio and flow rate of the suspension. A detailed description of the specific influence of each of these parameters can be found elsewhere (Holzner et al., 2017). Current experiments were carried out in a 500 ppm/1 MDa PEO and 1,000 ppm/1 MDa PEO (Sigma-Aldrich, Buchs, Switzerland) solutions for cells and yeast/beads, respectively. A stock solution at a concentration of 10,000 ppm was prepared and aged at room temperature for a month, to ensure stability (Holzner et al., 2017). The stock solution was diluted with DPBS (Life Technologies, Zug, Switzerland) to the desired concentration and used immediately or stored at 4°C.

The cell suspension was loaded into a 1 mL syringe (Gastight Syringes, Hamilton Laboratory Products, NV, USA) and delivered at flow rates of up to 240 μL/minute using a precision syringe pump (neMESYS, Cetoni, Korbussen, Germany). Settling of cells within syringes was minimized by matching the density of the medium to the cell suspension using a 36% v/v Optiprep Density Gradient Medium. A commercial calibration kit (Quantum Alexa Fluor 488 MESF, Bangs Laboratories, Indiana, USA) consisting of five microsphere populations (surface) labeled with increasing amounts of a specified fluorochrome, was used for intensity calibration measurements (Figures S4A and S4B). The volumetric flow rate of the cell suspension was adjusted, to ensure oversampling of cells during the imaging process and thus yield blur-free images according to relations presented in Figure S2A. Since the ROI is slightly larger than the diameter of the cell, oversampling allows us to image the same cell twice, ensuring the precise measurement of both size and content. This is achieved by synchronizing the cell velocity with the camera acquisition rate. The image acquisition rate was set to between 2,000 and 4,888 frames/s, depending on the magnification of the objective and the corresponding size of the region of interest. Accordingly, each cell traverses the microfluidic channel in a time period less than 500 μs and thus will be imaged more than once during the acquisition process. Using such criteria, cells should move at a linear flow velocity of between 0.03-0.05 m/s, depending on the magnification. Crucially, the number of cells detected in each frame is maximized by working at cell concentrations high enough to ensure compact packing (Holzner et al., 2017).

Optical setup & data acquisition

The optical system (Figure 1A) consists of an inverted microscope (Eclipse Ti-E, Nikon, Zurich, Switzerland) equipped with a motorized stage (Mad City Labs, Maddison, USA) and a Dual-View detection system (Cairn Research, Faversham, Kent, UK). The outputs of a green (561 nm, Coherent Genesis MX, Glasgow, UK) and blue (488 nm, Coherent Genesis MX, Glasgow, UK) laser were combined using a set of mirrors. After transmission through an acousto-optical tunable filter (AOTF nC-400-650-TN, AA Opto-electronic, Orsay, France) connected to a RF driver (AA Opto-electronic, Orsay, France), the combined beam was focused to a line with a width approximately equal to the average cell diameter (~15 μm) using a cylindrical lens (LJ1558RM-A, Thorlabs, Lübeck Germany). Yeast experiments required the use of an acylindrical lens (AYL2520-A, Thorlabs, Lübeck Germany) to generate a line width of 5 μm.

A variety of objective lenses, including a 10x (Plan Fluor 10x, NA 0.5, Nikon, Zurich, Switzerland), a 20x (Plan Apo 20x, NA 0.50, Nikon, Zurich, Switzerland) and a 40x (Plan Fluor 40x, NA 0.75, Nikon, Zurich, Switzerland) were used. Additionally, an extra lens that provided 1.5x magnification at the output port of the microscope was also used on occasion. Fluorescence originating from individual cells was collected by the objective lens and passed through the Dual-View optical configuration to obtain dual color images. Simultaneous bright-field and fluorescence imaging was accomplished using a red LED light source (Spectra X, Lumencor, Beaverton, USA) in combination with the blue laser at 488 nm, as depicted in Figure S4H.

The Dual-View optical configuration was mounted between the tube lens of the microscope and a CMOS camera (ORCA-flash 4.0, Hamamatsu, Solothurn, Switzerland or Prime 95B Scientific CMOS Camera, Roper Scientific, Planegg, Germany) and comprised two mirrors, a dichroic mirror and two emission filters. For dual color experiments, a dichroic mirror (HC BS 560, AHF, Tubingen, Germany) was used to split the emission light into two colors. Two emission filters 520/35 (F37-520, AHF, Tubingen, Germany) and 590 LP ET Longpass (F47-591, AHF, Tubingen, Germany) were used to detect mNeonGreen and mRuby2 fluorescence, respectively.

The two fluorophores were imaged simultaneously in different regions of the CMOS camera and commercial software (MicroManager 1.4.15, University of California, San Francisco, USA) used to record the images. For bright-field experiments, the longer wavelength channel was used without an emission filter. Synchronization of both the laser and the LED light source with the camera was accomplished using two ESIO AOTF controllers (ESImaging, Kent, UK). The AOTF and the LED were triggered by the CMOS camera with a TTL pulse (matched to the exposure time of the camera) to achieve synchronization between the laser (SPECTRA X light engine, Lumencor, USA) and the camera. The sampling frame rate of the ORCA-flash 4.0 CMOS camera was up to 4,888frames/s, and the AOTF driver generated a pulse length that varied between 13 and 20 μs (depending on the flow rates used) for both laser lines. The laser beam was modified into a slit-shaped profile, oriented orthogonally to the flow direction, through the use of a cylindrical lens. Using this excitation profile, only a narrow field needs to be illuminated. This contrasts with traditional epi-illumination excitation formats, in which the entire field of view is illuminated. The light density provided by the cylindrical lens increases the effective illumination intensity by one order of magnitude when compared to normal epi-illumination modalities.

Static images from relief phase and green channels (ex: 482/18 nm, em: 532/59 nm) from adherent 293T cells expressing different fluorescent proteins were acquired using a Floid Cell imaging station (Life Technologies, Zug, Switzerland) and saved as TIFF files.

Optimization of the illumination pulse duration and flow velocity for blur-free imaging

High-speed imaging in flow aims to extract precise information about cell size and morphology. It is therefore important to image with the highest temporal and spatial resolution. The flow rate determines the cell velocity in the microfluidic channel; however, if the object of interest is moving rapidly, the image may be susceptible to motion-blur. This undesired effect causes a smeared appearance of the imaged object. Minimizing motion-blur is needed to accurately capture a high-resolution image of a moving object and can be achieved by adjusting the temporal resolution of the imaging system, through control of the illumination pulse width or the flow rate. In the current configuration, the 500 μs exposure time refers to the camera exposure, while the laser strobing time (or pulse length) varies between 13 and 20 μs and defines the "effective exposure.

The relationship between the illumination pulse duration, flow velocity and motion blur is depicted in Figure S2B. The motion blur is given by the distance that a cell travels during the illumination duration. As expected, motion blur increases (at a given flow velocity) with the illumination pulse duration. If D is the displacement (in microns) of a cell moving with a velocity v during time t (the shutter speed), the motion blur is given as $D = t \times v$. This relationship can be used to define the ideal experimental parameters. Figure S2B presents the relationship between shutter time and cell velocity at fixed values of motion blur. A high cellular velocity means that a large number of cells move through the system and must be imaged using an exposure time that eliminates motion blur, while collecting as many fluorescence photons as possible. The "motion blur" lines shown in Figure S2B define a parameter space for a given experiment. In the current experiments, we aimed for a motion blur less than 0.5 μm; a value smaller than the diffraction limit of the 20X 0.50NA (0.55 μm) objective used in image colocalization studies. Indeed, no motion blur is evident in the acquired images and thus we are able to accurately quantify the size and the localization of spots

Sensitivity of the microfluidic imaging flow cytometer

We evaluated the sensitivity and detection range of our imaging flow cytometer using suspensions of fluorescent particles, characterized by four distinct fluorescence intensities. Based on the analysis of such calibration samples we are able to quantify our sensitivity, which is depicted in the calibration curve show in Figure S4B. Absolute quantification of the fluorescence intensity in MESF (molecules of equivalent soluble fluorophore FITC) units was provided by the manufacturer (Quantum Alexa Fluor 488 MESF, Bangs Laboratories, Indiana, USA). Fluorescence intensities ranged between 3,179 and 333,766 MESF units. The smallest intensity peak in our calibration curve (population 1, green histogram: Figure S4C) has an intensity of 3,179 MESF units. This intensity lies below the calculated limit of detection (LOD) (Armbruster and Pry, 2008)) of the imaging cytometer, which corresponds to 8,481 MESF. Interestingly, we were still able to detect beads with an intensity of 3,179 MESF units by bandpass filtering the images and integrating pixels with an intensity above the background. It is also noteworthy that most applications in flow cytometry typically exhibit values above 30,000 MESF (Wang et al., 2002).

Tradeoff between detection sensitivity and throughput

To provide a better assessment of the capabilities of the imaging flow cytometer, it is important to account for the trade-off between throughput and detection sensitivity using 15x magnification optics. In this regard it is important to realize that when acquiring images of rapidly moving objects, motion blur and noise are strictly controlled by the exposure time. The trade-off between long exposure times (that reduce the noise but increase motion blur) and short exposure times (that reduce motion blur at the cost of increasing noise and reducing the number of collected photons) is unavoidable. According to Mikami et al. the signal-to-noise ratio associated with a fluorescence image can be calculated using the signal-to-noise ratio of the camera readout per pixel (Mikami et al., 2020). The fluorescence signal (FS) expressed as the number of electrons is given by,

$$FS = P\,S^{-1}t\,N\,A\,\,\varphi\,n_{IFC}\,q_S = P\,S^{-1}D_x V^{-1}N\,A\,\,\varphi\,n_{IFC}\,q_S$$

Here, P is the power of the excitation beam, S the cross section of the excitation beam, t the time a molecule spends in the excitation beam, N the number of fluorescent molecules in a single-pixel area, A the absorption cross section of the fluorescent molecule, φ the

fluorescence quantum yield of the molecule, n_{IFC} the photon collection efficiency of the imaging platform, q_S the quantum efficiency of the camera sensor, D_x the distance traveled by the fluorescent molecule and V velocity of the fluorescent molecule. The experimental values of these parameters can be found in Table S1.

The Signal-to-Noise Ratio (SNR) is defined according to the following equation:

$$SNR = \frac{FS}{\sqrt{FS + \sigma^2}}$$

where σ is the readout noise of the image sensor. It is important to note that the SNR strongly depends on the number of fluorescence molecules within the object being imaged. The estimated fluorescence SNR is inversely proportional to the velocity/throughput of the fluorescent molecules as shown in Figure S4E (assuming 300 molecules per pixel). The increasing imaging speed comes at the expense of sensitivity, since a shorter exposure is used to obtain images. The sensitivity of the presented platform will deteriorate significantly for velocities above 0.1 m/s (i.e., a throughput of ~40,000 cells/s) due to the limited illumination time (5 μs) needed to produce blur free images. In the case of fluorescence imaging, the intrinsic weakness of the fluorescence signals is the primarily limitation. When acquiring images of rapidly moving objects, the exposure time must be precisely controlled, since this controls the amount of blur and noise in an observation. In the current scenario, the combination of a powerful light source modulated at high frequency and a high fluorescence quantum efficiency allows for blur-free imaging with excellent sensitivity. Optimal conditions for our system are achieved at velocities of 0.05 m/s.

QUANTIFICATION AND STATISTICAL ANALYSIS

Image processing and data analysis of imaging flow cytometry images

Post-processing of data is performed using algorithms that analyze fluorescence and bright-field images to extract the size, location and the intensity of cells and intracellular features. The image processing algorithm was implemented in Python 2.7 and OpenCV 2.4. The images acquired (and stored as a TIFF stack) were analyzed for various cellular attributes, including cell area, cell size, cell position, spot number, spot size, spot location, and fluorescence intensity. Data obtained from the processing algorithm were then plotted as scatterplots and histograms. Initially, the image is read from the TIFF stack and a "de-noising" algorithm is implemented in Python to perform intensity-based filtering of noise from the image (Crocker and Grier, 1996). This step is important as it reduces background noise and makes subsequent binary thresholding more reliable. An inbuilt OpenCV function '*findContours*' is then used to identify cell and spot borders, with each of the cell and spot images being stored as a closed contour. This closed contour provides cell and spot morphology parameters such as cell area, cell size and centroid coordinates. Using the cell border information, the raw image is analyzed for fluorescence. The built-in function '*pointPolygonTest*' allows assignment of spots to cell contours. The code searches for the maximum fluorescence intensity inside the defined cell area and also computes the mean fluorescence intensity of the cell.

The analysis of all images in a stack, gives a data matrix containing information on the size, area, cell centroid and fluorescence intensity of the cell. These raw data are then filtered to remove artifacts due to image noise and cell debris. The filtered data are then presented in the form of scatterplots and histograms. The CVs (coefficients of variation) were defined as the ratio of the standard deviation to the mean for a measured population.

For multi-parametric detection, it is essential to correlate co-localized events (for example, mRuby2-AGO2 and mNG-AGO2). This is achieved using the information derived from the coordinates of the centroid of the detected event. First data obtained from different detection channels are corrected for offsets in the position of detected event in the image. Subsequently, images from both channels are analyzed for cell or spot attributes. Detected events are then correlated by comparing the coordinates of the detected events in both channels. Once the events are correlated, plots of the chosen attributes can be generated.

Image processing and data analysis of static images

For each acquisition, processing masks were defined to segment each individual cell, and then corresponding images were extracted as a TIFF stack. The number of granules per cell were manually quantified by a human operator using more than 1000 cells per experimental conditions.

Flow cytometry and analysis

A commercial flow cytometer (Astrios MoFlo, San Jose, USA) was used for measuring the coefficient of variation (CV) of fluorescence intensity of Jurkat cells. Data were analyzed using R (www.r-project.org). A plot of forward scatter against side scatter was first used to gate cellular events and eliminate events caused by cell debris. A plot of peak area against peak height for the given detection channel was used to gate single cells. Finally, fluorescence intensity histograms were created for the cell population. The number of gated events corresponds to 20,000 cells for statistical robustness in data analysis.

ANOVA statistical analysis

To test for significant differences in the correlation coefficient between two different samples, one-way ANOVA analysis was performed using Prism 8 (Graphpad, San Diego) using multiple comparison test and Tukey correction using statistical hypothesis testing.